

## How Does Latent Cooling Affect Baroclinic Development in an Idealized Framework?

KRISTINE F. HAUALAND AND THOMAS SPENGLER

*Geophysical Institute, University of Bergen, and Bjerknes Centre for Climate Research, Bergen, Norway*

(Manuscript received 21 December 2018, in final form 5 June 2019)

### ABSTRACT

Latent cooling by evaporating or melting hydrometeors has recently been shown to contribute to the positive low-level potential vorticity (PV) anomaly below the layer of latent heating in midlatitude cyclones. While the low-level PV anomaly might be intensified by latent cooling, the influence on the overall baroclinic development remains unclear. Including both latent heating and cooling in the Eady model, this study finds that latent cooling reduces baroclinic growth. While the PV anomaly between the layers of latent cooling and heating increases for realistic heating intensities, the PV anomaly at the top of the heating layer decreases, as latent heating is weakened because of reduced vertical motion within the cyclone. Consequently, the relative contribution from diabatic heating to the generation of eddy available potential energy decreases when latent cooling is included. Thus, despite the recently emphasized role of evaporation for the low-level PV anomaly in developing cyclones, the overall effect of latent cooling is detrimental to baroclinic growth.


### 1. Introduction

Latent heating has been shown to increase the growth rate of midlatitude cyclones while their horizontal scale is reduced (e.g., Manabe 1956; Craig and Cho 1988; Snyder and Lindzen 1991; Moore and Montgomery 2004). Although latent heating is probably the most important diabatic effect on midlatitude cyclone development, Forbes and Clark (2003) and Dearden et al. (2016) reported significant latent cooling rates from sublimation, melting, and evaporation of hydrometeors in midlatitude cyclones. While many studies have investigated the effect of these cooling processes on mesoscale systems, such as fronts or sting jets (e.g., Huang and Emanuel 1991; Clough and Franks 1991; Parker and Thorpe 1995; Barth and Parsons 1996; Martínez-Alvarado et al. 2010), only a few have addressed the effect on synoptic-scale cyclones (e.g., Joos and Wernli 2012; Crezee et al. 2017). The latter studies found that latent cooling, in particular through evaporation of rain, contributes to the low-level potential vorticity (PV) anomaly within the cyclone. The

influence of this PV modification on cyclone development, however, remains unclear and forms the basis of this study.

Baroclinic instability is characterized by PV anomalies lying stationary relative to each other on the upper and lower boundaries (Bretherton 1966; Hoskins et al. 1985). These PV anomalies can be described as two phase-locked counterpropagating Rossby waves (e.g., Hoskins et al. 1985; Heifetz et al. 2004). De Vries et al. (2010) extended this framework to include interactions with PV anomalies induced by latent heating and emphasized the importance of the PV anomaly at the top of the heating layer. While its importance was supported by Pomroy and Thorpe (2000), other studies stressed the significance of the diabatically induced low-level PV anomaly for cyclone intensification (e.g., Davis and Emanuel 1991; Stoelinga 1996; Ahmadi-Givi et al. 2004). As the low-level PV anomaly is enhanced through evaporation or melting below the heating layer, the role of latent cooling on the interacting PV anomalies and the overall baroclinic development demands further assessment.

The influence of latent cooling on midlatitude cyclone development can also be explored by investigating

 Denotes content that is immediately available upon publication as open access.

Corresponding author: Kristine F. Haualand, kristine.haualand@uib.no



This article is licensed under a Creative Commons Attribution 4.0 license (<http://creativecommons.org/licenses/by/4.0/>).

TABLE 1. Dimensional and nondimensional values of model parameters with corresponding units.

Parameter	$S$	$\lambda$	$f$	$p_t$	$p_b$
Dimensional value	$0.04 \text{ m}^2 \text{ s}^{-2} \text{ hPa}^{-2}$	$35 \text{ m s}^{-1} \text{ hPa}^{-1}$	$10 \text{ s}^{-1}$	$150 \text{ hPa}$	$1000 \text{ hPa}$
Nondimensional value	4	3.5	1	0.15	1

the energetics. While no studies have looked at the direct influence from latent cooling on the diabatic generation of eddy available potential energy (EAPE), several studies have found that latent heating is the most important positive contributor to the EAPE in midlatitude cyclones (e.g., Vincent et al. 1977; Lin and Smith 1979; Smith 1980). Furthermore, diabatic heating not only generates EAPE; it also enhances the conversion to kinetic energy by strengthening the secondary circulation within the cyclone (Robertson and Smith 1983). The complexity of this direct and indirect impact on the energetics motivates a more detailed analysis of the role of latent heating and cooling.

We investigate the influence of latent cooling on the energetics, PV distribution, and baroclinic growth using a diabatic extension of the quasigeostrophic (QG) Eady (1949) model. The original extension was developed by Mak (1994) and included only latent heating. We add latent cooling at lower levels, which can be interpreted as evaporation of rain, snowmelt, and sublimation. Similar to Mak (1994), we use a highly idealized vertical distribution of latent heating and cooling, though we also test the validity of our results by prescribing more realistic profiles and by changing the basic-state static stability to mimic the effect of mixing in the heating and cooling layers.

## 2. Model

### a. Model equations

We focus on the incipient stage of baroclinic development and use the same QG linear model and two-dimensional  $(x, p)$  coordinate system as Mak (1994), where  $x$  and  $p$  define the horizontal and pressure coordinates, respectively, but we allow the diabatic effects to include both latent heating and cooling. Thus, the diabatic processes can represent condensation and evaporation of rain as well as other phase transitions such as freezing, deposition, snowmelt, and sublimation. We start with the nondimensionalized QG  $\omega$  and PV equations

$$\frac{\partial^2 \omega}{\partial p^2} + S \frac{\partial^2 \omega}{\partial x^2} = -2\lambda \frac{\partial^3 \psi}{\partial x^3} - \frac{\partial^2}{\partial x^2} \left( \frac{Q}{p} \right) \quad (1)$$

and

$$\left( \frac{\partial}{\partial t} + \bar{u} \frac{\partial}{\partial x} \right) q + \frac{\partial \psi}{\partial x} \frac{\partial}{\partial p} \left( \frac{\lambda}{S} \right) = -\frac{\partial}{\partial p} \left( \frac{Q}{Sp} \right), \quad (2)$$

where

$$q = \frac{\partial^2 \psi}{\partial x^2} + \frac{\partial}{\partial p} \left( \frac{1}{S} \frac{\partial \psi}{\partial p} \right)$$

is the QG PV,  $\psi$  is the QG streamfunction,  $\omega$  is the vertical motion in pressure coordinates,  $\lambda$  is the vertical wind shear,  $\bar{u}$  is the basic-state zonal wind,  $Q$  is the diabatic heating rate, and  $S$  is the basic-state static stability. The dimensional form of  $S$  is defined as

$$S = -\frac{R}{p} \left( \frac{\partial T_0}{\partial p} - \frac{RT_0}{c_p p} \right),$$

where  $R$  is the gas constant,  $c_p$  is specific heat at constant pressure, and  $T_0$  is the background temperature. For consistency, we choose the same parameter values as Mak (1994) (see Table 1), where the velocity and length scales are  $U = 10 \text{ m s}^{-1}$  and  $L = 10^6 \text{ m}$ , respectively. For constant  $\lambda$ ,  $\bar{u}(p) = \lambda(p_b - p)$  increases linearly with height (Fig. 1).

Assuming  $\omega = 0$  at the top ( $p = p_t$ ) and bottom ( $p = p_b$ ) of the model boundaries yields the vertical boundary condition for the thermodynamic equation:

$$\left( \frac{\partial}{\partial t} + \bar{u} \frac{\partial}{\partial x} \right) \frac{\partial \psi}{\partial p} + \lambda \frac{\partial \psi}{\partial x} = -\frac{Q}{p}, \quad \text{at } p = p_t, p_b, \quad (3)$$

where  $-\partial \psi / \partial p$  is proportional to the negative density perturbation, but, consistent with previous literature, will hereafter be referred to as temperature.

Following Mak (1994), we further assume that  $\psi$  and  $\omega$  have wavelike solutions in the  $x$  direction:

$$[\psi, \omega] = \text{Re}\{[\hat{\psi}, \hat{\omega}] \exp[i(kx - \sigma t)]\}, \quad (4)$$

where  $k$  is the zonal wavenumber,  $\sigma$  is the wave frequency, and the hat denotes Fourier transformed variables.

### b. Parameterization of latent heating and cooling

We parameterize the diabatic forcing in the same way as Mak (1994):

$$\hat{Q} = -\frac{\varepsilon \tilde{h}(p)}{2} \hat{\omega}_{\text{hb}}(k), \quad (5)$$

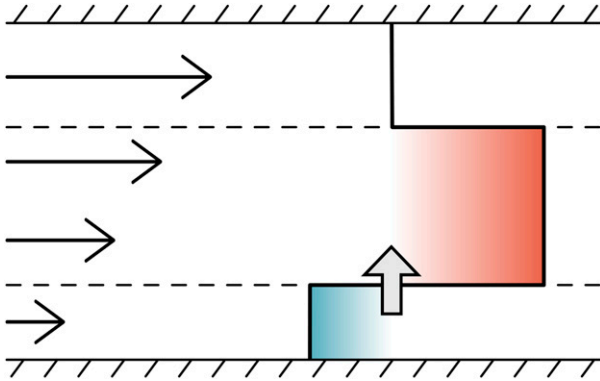


FIG. 1. Schematic of the heating and cooling layers, where red (blue) indicates heating (cooling). Black thin arrows illustrate the increase of wind with height. Gray thick arrow represents the vertical motion at the bottom of the heating layer, which is used in the heating parameterization. Dashed lines indicate boundaries where diabatic PV anomalies are induced.

where  $\varepsilon$  is the heating intensity parameter,  $\tilde{h}$  is the vertical heating profile, and  $\hat{\omega}_{hb}$  is the vertical motion at the bottom of the heating layer, as we assume heating is controlled by low-level convergence, similar to the idealized study by, for example, [Craig and Cho \(1988\)](#). The structure of the heating profile ensures a reasonable representation of the vertical distribution of diabatic heating in midlatitude cyclones and can be compared to case studies by, for example, [Dearden et al. \(2016\)](#).

The sign of  $\tilde{h}$  and  $\hat{\omega}_{hb}$  determines whether there is latent heating or cooling. A plausible physical reasoning for the diabatic cooling in the descent region is to assume a saturated atmosphere, where midlevel cooling represents longwave radiative cooling and evaporation of cloud droplets (e.g., [De Vries et al. 2010](#)). Furthermore, the low-level heating in the shallow layer below this cooling region could be associated with shallow convection in the cold sector.

For a conditional representation of heating, where condensational heating and evaporative cooling only occur in the ascent and not in the descent region, diabatic heating could be parameterized by an infinite spectral series. The unconditional heating in (5) would then represent the fundamental harmonic, while higher harmonics are neglected. H. de Vries (2019, personal communication) supports that such an unconditional representation of diabatic heating does not significantly alter the qualitative results at the incipient stage. We therefore argue that the heating parameterization in (5) is representative for the early development stage of extratropical cyclones.

Inserting (4) and (5) into (2) and (3) and letting  $h = \tilde{h}/p$ , hereafter referred to as the heating profile, yield

$$\frac{d^2 \hat{\omega}}{dp^2} - Sk^2 \hat{\omega} = i2\lambda k^3 \hat{\psi} - \frac{\varepsilon k^2}{2} h \hat{\omega}_{hb} \quad (6)$$

and

$$\begin{aligned} (\bar{u}k - \sigma) \left[ \frac{d}{dp} \left( \frac{1}{S} \frac{d\hat{\psi}}{dp} \right) - k^2 \hat{\psi} \right] + k \frac{d}{dp} \left( \frac{\lambda}{S} \right) \hat{\psi} \\ = -i \frac{\varepsilon}{2} \hat{\omega}_{hb} \frac{d}{dp} \left( \frac{h}{S} \right), \end{aligned} \quad (7)$$

with the corresponding boundary conditions  $\hat{\omega} = 0$  and

$$(\bar{u}k - \sigma) \frac{d\hat{\psi}}{dp} + i \frac{\varepsilon h}{2} \hat{\omega}_{hb} + \lambda k \hat{\psi} = 0 \quad \text{at } p = p_t, p_b. \quad (8)$$

As (6) is linear, the vertical motion can be split into two components forced by each of the terms on the right-hand side. [Mak \(1994\)](#) argued that although interpreting these components as the dynamic and diabatic vertical motion can be meaningful for weak to moderate heating intensities, it is important to keep in mind that the components are coupled through the streamfunction and heating parameterization. Thus, they are neither purely dynamic nor diabatic. Nevertheless, we refer to them as the dynamic ( $\omega_d$ ) and diabatic components, where the diabatic component can be further split into one component due to latent heating  $\omega_h$  and one due to latent cooling  $\omega_c$ .

To incorporate latent cooling in the heating profile, we modify the step function used by [Mak \(1994\)](#) to be negative below the heating layer:

$$\begin{aligned} h(p) &= H(p - p_{ht}) - (1 + \gamma)H(p - p_{hb}) \\ &= \begin{cases} 0 & \text{for } p < p_{ht} \\ 1 & \text{for } p_{ht} < p < p_{hb} \\ -\gamma & \text{for } p_{hb} < p \end{cases}, \end{aligned} \quad (9)$$

where  $p_{ht} = 0.4$  and  $p_{hb} = 0.9$  are the pressures at the top and bottom of the heating layer, respectively, and  $\gamma$  is the fraction of latent cooling below  $p_{hb}$  with respect to the amount of latent heating above. For example, if  $\gamma = 0.3$ , the heating profile is 1 within the heating layer and  $-0.3$  below, yielding latent heating (cooling) above (below) the bottom of the heating layer if  $\omega_{hb} < 0$  ([Fig. 1](#)). Note from (7) that for constant  $\lambda$  and  $S$ , interior PV anomalies can only exist where  $dh/dp \neq 0$ . Thus, the step function in (9) yields interior PV anomalies at the heating boundaries  $p_{ht}$  and  $p_{hb}$  only (dashed horizontal lines in [Fig. 1](#)).

Note that  $h(p)$  is the heating profile in the PV equation. The distribution of heating  $\tilde{h}(p)$  in *physical space* is

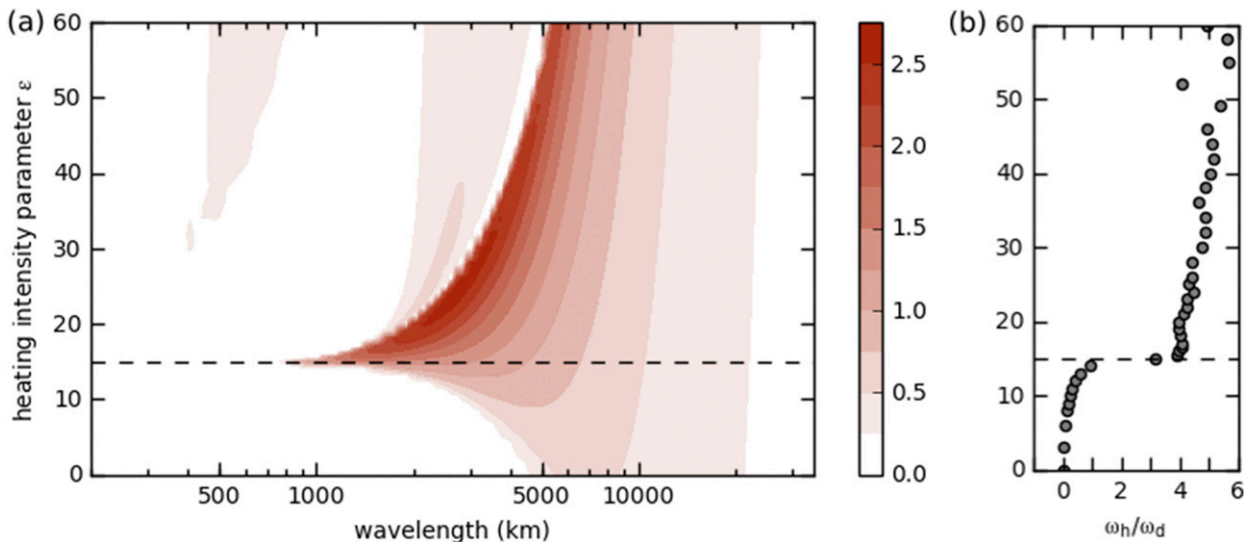


FIG. 2. (a) Growth rate ( $10^{-5} \text{ s}^{-1}$ ) vs wavelength (km) for varying heating intensity parameter  $\varepsilon$ . (b) Amplitude of vertical motion due to latent heating  $\omega_h$  divided by amplitude of dynamically induced vertical motion  $\omega_d$ , both taken at the bottom of the heating layer. Dashed horizontal lines mark where  $\varepsilon = 15$ .

obtained by multiplying (9) by pressure, yielding a linearly decreasing profile with pressure within the heating layer.

### c. Numerical solution

We use  $n = (p_b - p_t)/\Delta p + 1 = 120$  vertical levels, where  $\Delta p$  is the vertical increment between two grid points. Vertical derivatives are expressed with standard finite-difference methods, using forward and backward differences at the model and heating boundaries and central differences elsewhere. Using the heating profile prescribed in (9) together with the boundary conditions  $\omega = 0$  and (8), (6) and (7) form the eigenvalue problem

$$\mathbf{A}\xi = \sigma\mathbf{B}\xi, \quad (10)$$

where  $\mathbf{A}$  and  $\mathbf{B}$  are matrices of dimension  $2n \times 2n$ , the wave frequency  $\sigma$  is the eigenvalue, and  $\xi$  is the eigenvector representing  $\hat{\psi}(p)$  and  $\hat{\omega}(p)$  through all vertical grid points from 1 to  $n$ :

$$\xi = [\hat{\psi}_1, \hat{\psi}_2, \dots, \hat{\psi}_n, \hat{\omega}_1, \hat{\omega}_2, \dots, \hat{\omega}_n]. \quad (11)$$

Applying standard solution techniques using the geev routine in the Linear Algebra Package (LAPACK; Anderson et al. 1999), which is based on the numerical QR algorithm, (10) can be solved for  $\sigma$  and  $\xi$ . Hence, for a given wavenumber  $k$ , the full structure of  $\psi$  and  $\omega$  can be derived from (4). At least 1 degree of freedom exists for all nontrivial solutions of (10), implying that the eigenvector  $\xi$  is not scaled and that we cannot quantitatively compare  $\psi$  and  $\omega$  for different wavelengths and experiments. To alleviate this issue, we

tested several wavelength-dependent normalizations of  $\hat{\psi}$  and  $\hat{\omega}$  ranging from kinetic energy, available potential energy, total energy, minimum amplitude of the streamfunction, to the amplitude of the streamfunction at the surface. These normalizations allow for a more meaningful quantitative comparison of the solutions and yield important indications on how pertinent variables are influenced by diabatic effects. As we find similar behavior for all normalizations, we only present results normalized by total energy. Henceforth, all values except growth rate and wavelength are normalized with total energy, although not explicitly stated everywhere.

## 3. Choice of heating intensity and depth

### a. Impact of heating intensity on growth rate and wavelength

Before including the effect of latent cooling, we examine the limitations of our linear model. Because of the normalization issues outlined in the previous subsection, we can neither directly infer the absolute heating rate from the heating intensity, nor assess the absolute magnitude of the model variables. Nevertheless, using realistic estimates of  $\psi$  and  $\omega$ , we perform a scale analysis comparing the terms in the QG thermodynamic equation and contrast them with the term for ageostrophic advection of temperature, which is one order Rossby higher than the QG terms. When normalizing  $\psi$  and  $\omega$  with a factor that yields surface meridional wind perturbations of  $5 \text{ m s}^{-1}$ , we find that the magnitude of the ageostrophic

advection term is 25%–45% of the dominating QG terms when  $0 \leq \varepsilon \leq 30$  (not shown). For comparison, using surface wind perturbations of  $10 \text{ m s}^{-1}$ , the corresponding ratio for the dry Eady limit ( $\varepsilon = 0$ ) is 49%. We therefore argue that the inclusion of diabatic heating does not violate the QG approximation beyond what is regularly accepted in the dry Eady limit.

For  $\varepsilon \leq 15$ , an increase in  $\varepsilon$  yields an increase in the maximum growth rate and a decrease in the wavelength of the most unstable mode (Fig. 2a), consistent with several previous studies (e.g., Emanuel et al. 1987; Whitaker and Davis 1994; Moore and Montgomery 2004). As the wavelength of the instability is related to the vertical distance between the interacting PV anomalies (Hoskins et al. 1985), the decrease in wavelength for increasing  $\varepsilon$  is as expected because of the intensification of interior PV anomalies that acts to reduce the vertical distances between interacting PV anomalies. For  $\varepsilon > 15$ , the growth rate keeps increasing with increasing  $\varepsilon$  until  $\varepsilon = 24$ , although the wavelength is now also increasing. The latter indicates a regime shift, as it is in disagreement with the previously outlined arguments and findings. The implications of the regime shift are beyond the focus of this study.

*b. Diabatically and dynamically induced vertical motion and estimated heating rates*

The change in the qualitative behavior of the wavelength and the growth rate for  $\varepsilon > 15$  is likely related to the dominance of the vertical motion due to latent heating  $\omega_h$  compared to the dynamically induced  $\omega_d$  (Fig. 2b). This diabatic dominance is not common in midlatitude cyclones as shown in a statistical analysis by Stepanyuk et al. (2017), in a model simulation of the intense *Queen Elizabeth II* storm by Pauley and Nieman (1992), and in an idealized baroclinic wave simulation by Rantanen et al. (2017). Thus, heating intensities  $\varepsilon \leq 15$  seem to be most applicable to midlatitude cyclones.

Furthermore, using the scaling estimate by Mak (1994), a heating intensity parameter  $\varepsilon = 30$  corresponds to a heating rate of  $80 \text{ K day}^{-1}$ . This is significantly larger than in the intense midlatitude cyclones studied by Pauley and Nieman (1992) and Dearden et al. (2016), where the maximum heating rates are below  $20 \text{ K day}^{-1}$ . Even though Joos and Wernli (2012) showed a locally confined maximum heating rate above  $50 \text{ K day}^{-1}$  during the intensifying phase, the heating rate averaged over the heating layer was at least 2–3 times weaker. Moreover, Kuo et al. (1991) estimated heating rates up to  $550 \text{ K day}^{-1}$  in the explosive *Queen Elizabeth II* storm, albeit at a highly nonlinear stage with the heating confined to a narrow band of about 250 km and a limited amount of time. Thus, there exist extreme cases where the average

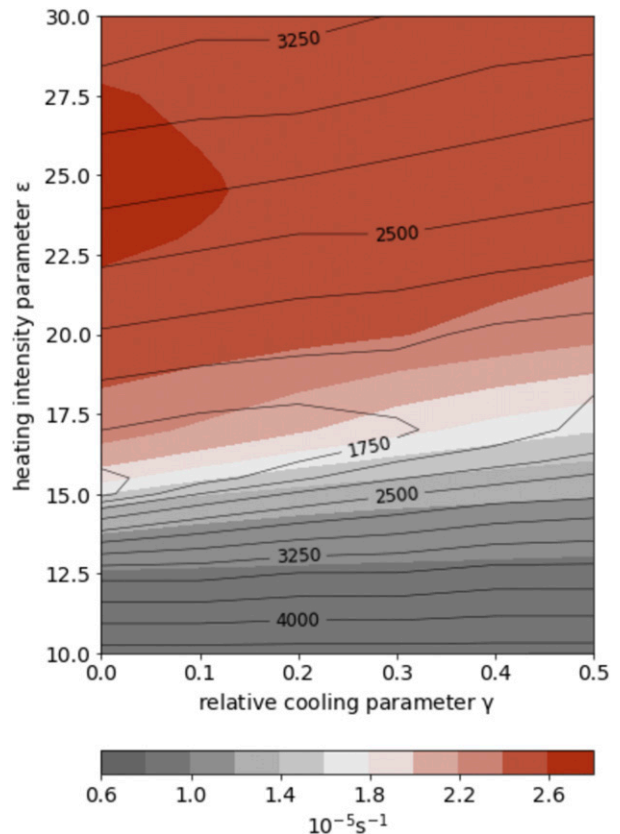


FIG. 3. Growth rate (shading,  $10^{-5} \text{ s}^{-1}$ ) and wavelength (contours, km) of the most unstable mode for various heating intensity parameter  $\varepsilon$  and relative cooling parameter  $\gamma$ .

heating rate exceeds  $100 \text{ K day}^{-1}$ , though these values can be argued to be rare and not representative for a larger area of the developing cyclone. We therefore argue that heating intensities corresponding to  $\varepsilon \leq 15$ , that is, heating rates  $\leq 40 \text{ K day}^{-1}$ , are a realistic and representative choice.

*c. Additional modes at strong heating intensities*

For  $\varepsilon > 15$ , additional unstable modes at shorter wavelengths appear, which were studied in detail by Mak (1994) (Fig. 2a and his Figs. 6b,c). The first of these modes appears for  $\varepsilon \geq 20$  and is confined to the layer above the heating layer, whereas the second mode appears for  $\varepsilon \geq 35$  and is confined to the layer below the heating layer. While Mak (1994) indicated that the lower mode can be associated with mesoscale cyclones such as polar lows, we argue that the mode’s shallow low-level westward tilt with height would be in the boundary layer where the atmosphere is commonly well mixed, as seen in the vertical cross sections of polar lows by Terpstra et al. (2015). Consequently, the suggested interaction between the PV anomalies at the surface and the

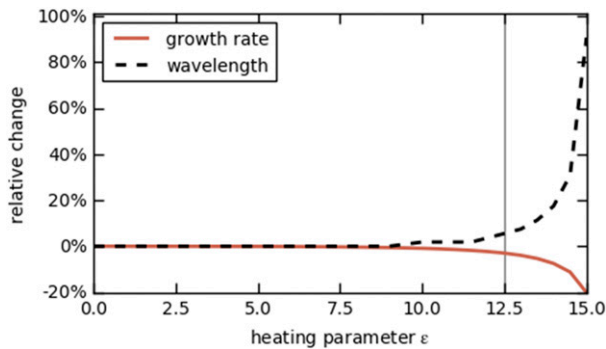


FIG. 4. Change in growth rate (red) and wavelength (dashed black) from  $\gamma = 0.0$  to  $\gamma = 0.5$  relative to the reference value at  $\gamma = 0.0$  for the most unstable mode and various heating intensity parameters  $\varepsilon$ . The gray vertical line marks where  $\varepsilon = 12.5$ .

bottom of the heating layer is an unlikely feature of polar lows. Similarly, because of the unrealistically strong heating intensities necessary for these additional modes, we also question whether the upper mode identified by Mak (1994) can be associated with realistic atmospheric instabilities. Considering the limited validity of these additional modes, the aforementioned unrealistic dominance of  $\omega_h$ , as well as the excessive estimated heating rates for large  $\varepsilon$ , we restrict our study to  $\varepsilon \leq 15$ .

#### d. Justification for chosen heating boundaries

Based on a subjective evaluation of vertical heating distributions in case studies of representative midlatitude cyclones (Pauley and Nieman 1992; Joos and Wernli 2012; Joos and Forbes 2016; Dearden et al. 2016), we find the bottom of the heating layer to be approximately between 950 and 800 hPa, and the top of the heating layer to be roughly between 500 and 300 hPa. Thus, our choice using the same heating boundaries as Mak (1994), where  $p_{hb} = 900$  hPa and  $p_{ht} = 400$  hPa, appears reasonable.

#### e. Impact from latent cooling

For increasing latent cooling, the wavelength of the most unstable mode increases at heating intensities  $10 \leq \varepsilon \leq 15$ , but decreases at intensities  $18 \leq \varepsilon \leq 30$  (Fig. 3). In this range of heating intensities, the maximum growth rate decreases with increasing latent cooling. Comparing Fig. 3 with Fig. 2a, the effects of latent cooling are similar to the effect of decreasing  $\varepsilon$ . This relation between an increase in  $\gamma$  and a decrease in  $\varepsilon$  remains similar when examining the additional modes appearing at extreme heating intensities (not shown).

The changes in wavelength and growth rate for increasing latent cooling depicted in Fig. 3 increase exponentially for increasing  $\varepsilon$  (Fig. 4, shown only up to  $\varepsilon = 15$ ).

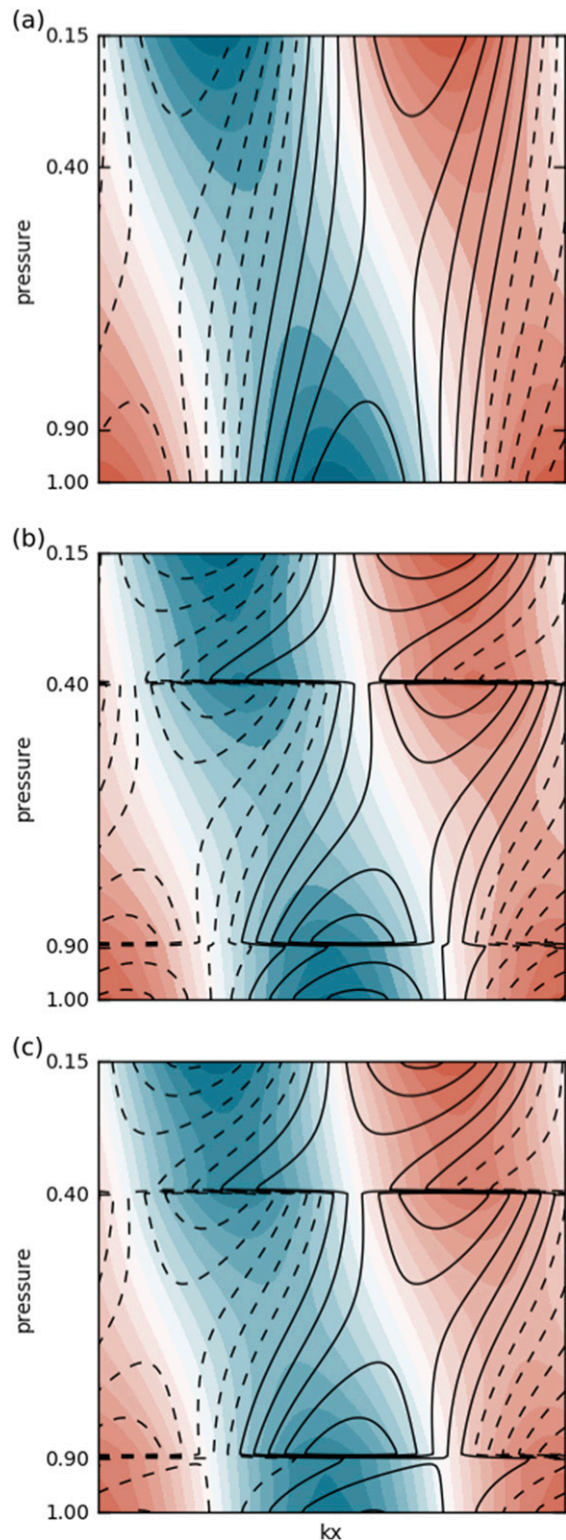


FIG. 5. Structure of streamfunction (shading) and  $-\partial\psi/\partial p \propto$  temperature (contours) for the most unstable mode for (a)  $\varepsilon = 0$  and  $\gamma = 0.0$  (dry Eady mode), (b)  $\varepsilon = 12.5$  and  $\gamma = 0.0$ , and (c)  $\varepsilon = 12.5$  and  $\gamma = 0.5$ . Solid (dashed) contours and red (blue) shading represent positive (negative) values.

To investigate cases with a clear contribution from latent cooling, but at the same time staying clear of the threshold at  $\varepsilon = 15$ , we focus our analysis on  $\varepsilon = 12.5$ . At this heating intensity, the growth rate decreases by 3.0% and the wavelength increases by 5.3% when increasing  $\gamma$  from 0.0 to 0.5. The corresponding values if using  $\varepsilon = 10$  are 0.9% and 1.3%, respectively.

#### 4. Impact from latent heating and cooling on structure and amplitude

##### a. Streamfunction and temperature

Despite the noteworthy impact from latent heating and cooling on the growth rate, the structure of the streamfunction remains qualitatively similar to the dry Eady solution (Fig. 5a) when including latent heating (Fig. 5b) or when including both latent heating and cooling (Fig. 5c). It is particularly striking that there is barely any change in structure when adding latent cooling (Fig. 5c) to the results including latent heating (Fig. 5b). All solutions tilt westward with height, in accordance with baroclinic instability. The main difference is the presence of local extrema and weak kinks at the heating boundaries when adding latent heating and/or cooling. The meridional velocity  $\partial\psi/\partial x$  is proportional to the streamfunction and phase shifted by  $90^\circ$  (not shown).

As expected from baroclinic instability theory, the structure of the temperature (contours in Fig. 5) tilts eastward throughout the whole model troposphere. When including latent heating and/or cooling, local temperature extrema are present within the heating layer and close to the heating boundaries. The sign of the temperature anomalies partly reverses across the heating boundaries, especially when  $\varepsilon \rightarrow 15$  (not shown). This temperature reversal is consistent with the strengthening of the diabatic PV anomalies (not shown), where a positive (negative) PV anomaly is associated with warm (cold) air above and cold (warm) air below. Such a PV dipole is a common feature of the early development stage of midlatitude cyclones (e.g., Crezee et al. 2017).

##### b. Interior PV anomalies and diabatic heating

With  $\varepsilon = 12.5$  and  $\gamma = 0.0$ , the amplitude of the PV anomalies at the top of the heating layer (blue stars in Fig. 6a) is almost twice as large as the PV anomalies at the bottom of the heating layer (red stars). As  $\gamma$  increases, the PV anomalies at the top of the heating layer weaken while the PV anomalies at the bottom of the heating layer strengthen. This response is in accordance with the increase in the heating step at the bottom of the heating

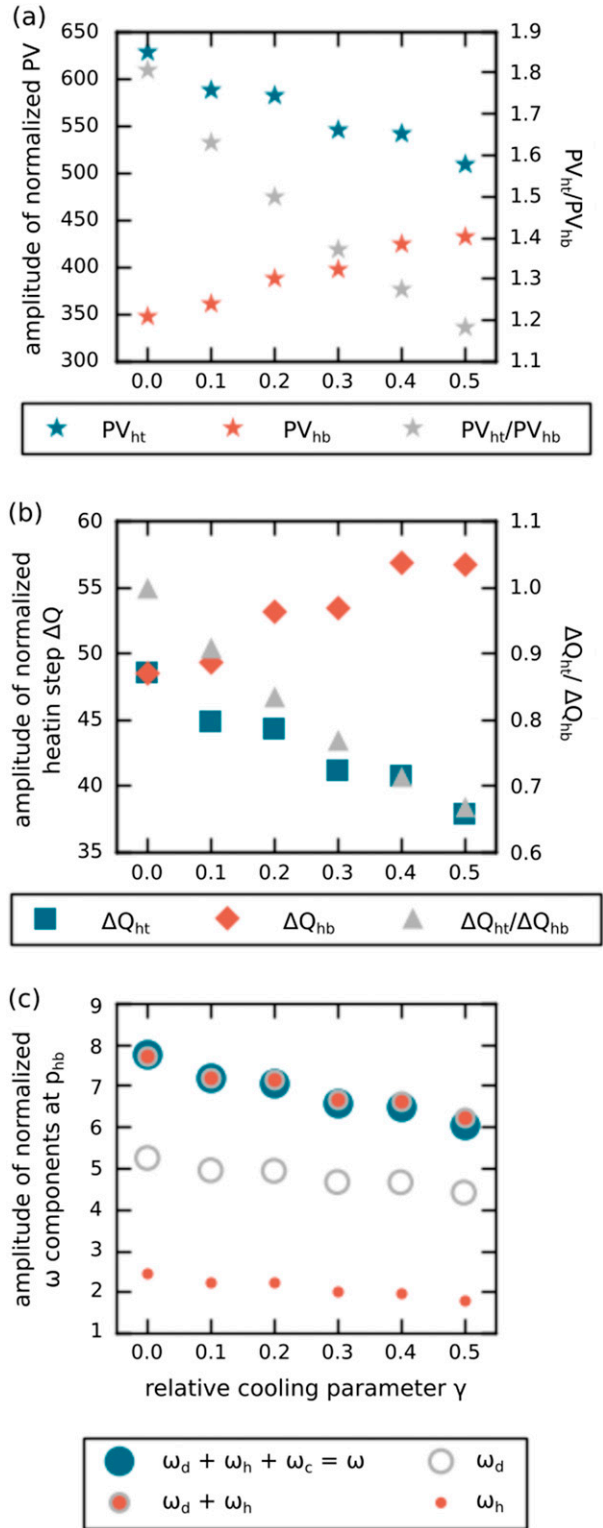


FIG. 6. (a) Amplitude of the PV anomalies at the top (blue) and bottom (red) of the heating layer and their relative amplitudes (gray). (b) Amplitude of the vertical difference of diabatic heating  $\Delta Q$  around the top (blue) and bottom (red) of the heating layer and their relative amplitudes  $\Delta Q_{ht}/\Delta Q_{hb}$  (gray). (c) Amplitude of  $\omega_d$  (gray circles),  $\omega_h$  (red dots),  $\omega_d + \omega_h$  (red dots with gray circles), and  $\omega = \omega_d + \omega_h + \omega_c$  (blue), all taken at the bottom of the heating layer. All quantities are nondimensional and normalized with respect to total energy and are shown for  $\varepsilon = 12.5$  with varying relative cooling parameters  $\gamma$ .

layer and the decrease in the heating step at the top of the heating layer for increasing  $\gamma$  (Fig. 6b). The decrease of the heating step at the top of the heating layer must be related to reduced vertical motion, because that is the only parameter in the heating parameterization that is not fixed. Such a reduction in vertical motion has also an impact on the heating step at the bottom of the heating layer, but as latent cooling is added below the heating layer, there can still be a net increase of the heating step at this level.

The decrease in the PV anomalies at the top of the heating layer *relative* to the PV anomalies at the bottom of the heating layer (gray stars for  $\varepsilon = 12.5$  in Fig. 6a) remains when examining other heating intensities where  $\varepsilon \leq 15$ . The *absolute* change of the PV anomalies, however, depends on the relation between the reduction of midlevel latent heating and the increase in low-level latent cooling, which varies with heating intensity. For example, when  $\varepsilon \rightarrow 15$ , latent cooling weakens the diabatic PV anomalies at *both* levels, though more the upper anomalies than the lower anomalies (not shown), because the reduction of latent heating overcompensates the increase in the heating step at the bottom of the heating layer because of latent cooling. For weak heating intensities ( $\varepsilon \rightarrow 0$ ), however, the reduction of latent heating by latent cooling is negligible and the PV anomalies at the top of the heating layer barely change for increasing latent cooling while the increase in the PV anomalies at the bottom of the heating layer is enhanced (not shown).

### c. Diabatic heating and vertical motion

The zonal distribution of diabatic heating (contours in Fig. 7) is determined by the vertical motion at the bottom of the heating layer (shading in Fig. 7) and is mostly positioned in the warm and ascending southerly flow. This placement is consistent with midlatitude cyclones, where the primary cloud-producing flow is in the warm conveyor belt (e.g., Browning 1990).

The structure of the vertical motion remains similar when including latent heating and/or cooling and is mostly determined by the dynamic component  $\omega_d$  (shading in Fig. 8). However, when diabatic effects are included, there is also a significant contribution from the component due to latent heating  $\omega_h$  (black contours in Fig. 8). The amplitudes of both  $\omega_d$  and  $\omega_h$  at the bottom of the heating layer decrease when adding latent cooling (gray circles and red dots in Fig. 6c, respectively), contributing to a net decrease in the total vertical motion at this level (blue dots in Fig. 6c). This decrease in vertical motion is in accordance with a case study of midlatitude cyclones by Martínez-Alvarado et al. (2016) and with the decrease in absolute latent

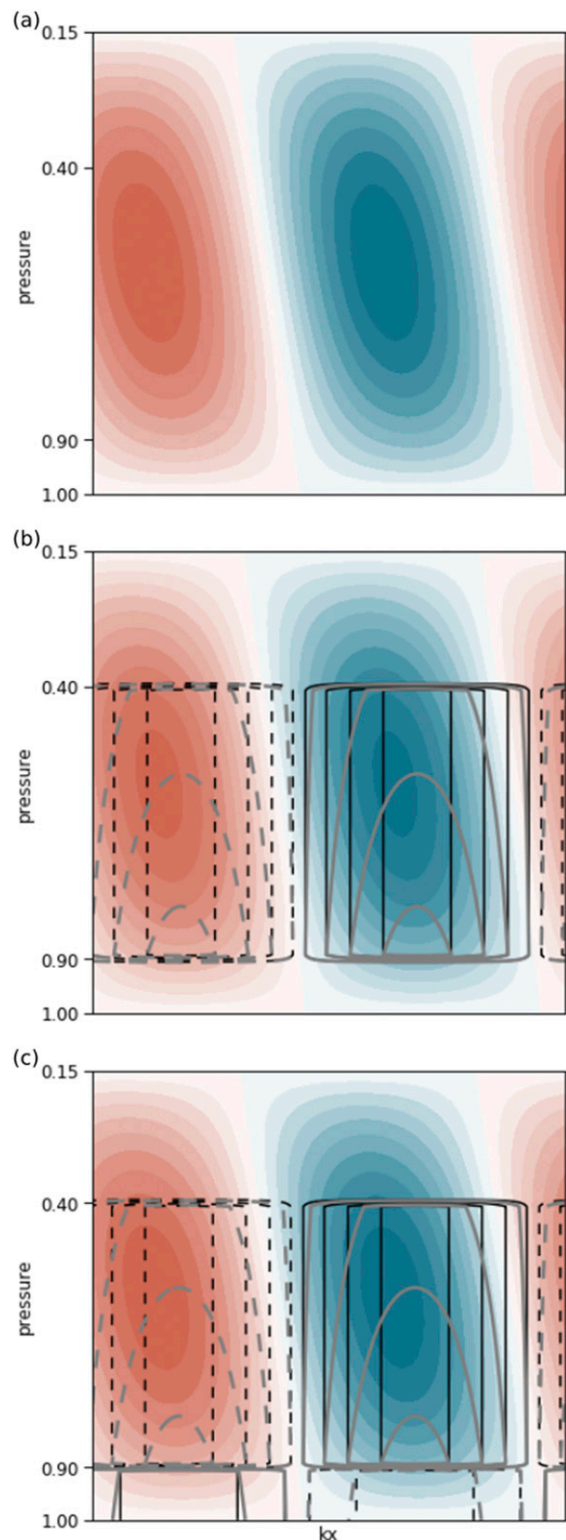


FIG. 7. As in Fig. 5, but for vertical motion (shading) and diabatic heating based on  $h$  (black contours) and  $\hat{h}$  (gray contours).



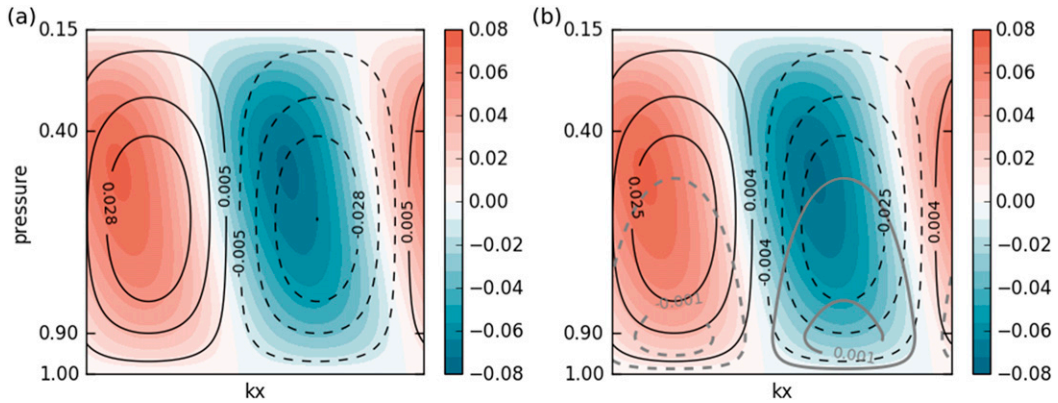


FIG. 8. Structure of the vertical motion components  $\omega_d$  (shading),  $\omega_h$  (black contours), and  $\omega_c$  (gray contours) for the modes in Figs. 7b and 7c.

heating in the presence of latent cooling, as discussed in section 4b.

In contrast to the other components of vertical motion  $\omega_d$  and  $\omega_h$ , the component due to latent cooling  $\omega_c$  increases when  $\gamma$  increases (not shown). However, since  $\omega_c$  is both weaker and nearly in antiphase compared to the other vertical motion components (gray contours in Fig. 8),  $\omega_c$  still contributes to a net reduction in vertical motion for increasing  $\gamma$ . This is evident when comparing the total vertical motion with the vertical motion that excludes  $\omega_c$  (blue dots and red dots with the gray edge in Fig. 6c), where 12% of the total reduction of vertical motion from  $\gamma = 0.0$  to  $\gamma = 0.5$  stems from  $\omega_c$ .

d. Relation between vertical motion and wavelength

As latent cooling is also related to increasing wavelengths (Fig. 3), the reduced vertical motion for increasing  $\gamma$  can also be related to the horizontal scale. For constant  $\gamma$ , an increase in wavelength is consistent with reduced vertical motion (Fig. 9), as expected from QG scaling  $\omega(\partial/\partial p) \sim (U/L)R_0$  (e.g., Holton and Hakim 2012), where  $R_0$  is the Rossby number. As long as  $\gamma$  is constant, this reduction with wavelength is true for all three components of  $\omega$  (colored lines in Fig. 9), and holds for other reasonable values of  $\varepsilon$  and  $\gamma$  (not shown). When  $\gamma$  increases, however, there is, as noted in section 4c, a net increase in  $\omega_c$ , despite the shift to longer wavelengths (not shown).

5. Energetics

To further elucidate the effect of latent cooling on baroclinic development we examine the diabatic contributions to the energetics. Following Lorenz (1955), the tendency of eddy available potential energy  $A_e$  can be expressed as

$$\frac{\partial A_e}{\partial t} = C_a + G_e - C_e, \tag{12}$$

where

$$C_a = -\frac{\lambda}{S} \overline{\psi_x \psi_p}, \quad G_e = -\frac{1}{S} \overline{Q \psi_p}, \quad \text{and} \quad C_e = \overline{\omega \psi_p} \tag{13}$$

represent the conversion from basic-state available potential energy to eddy available potential energy, the generation of eddy available potential energy from diabatic heating, and the conversion from eddy available potential energy to eddy kinetic energy, respectively. The bar denotes zonal and vertical averages. In this study, we split the diabatic term into components due to latent heating  $G_e^h$  and latent cooling  $G_e^c$ .

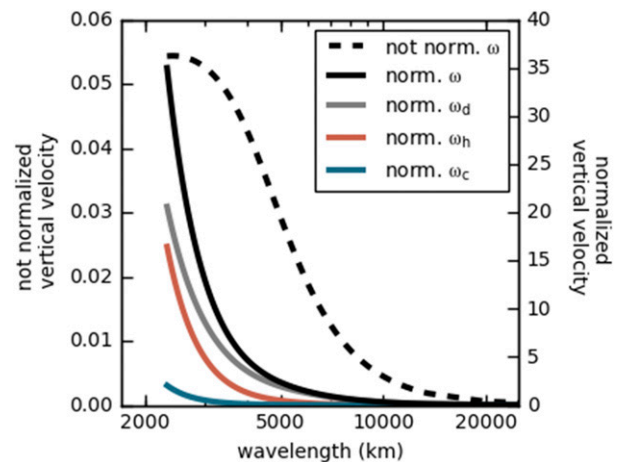


FIG. 9. Amplitude of nonnormalized (dashed) and normalized (solid) vertical motion at the bottom of the heating layer for  $\varepsilon = 12.5$ ,  $\gamma = 0.5$ , and varying wavelengths. Black lines show total vertical motion, whereas colored lines show the different components.

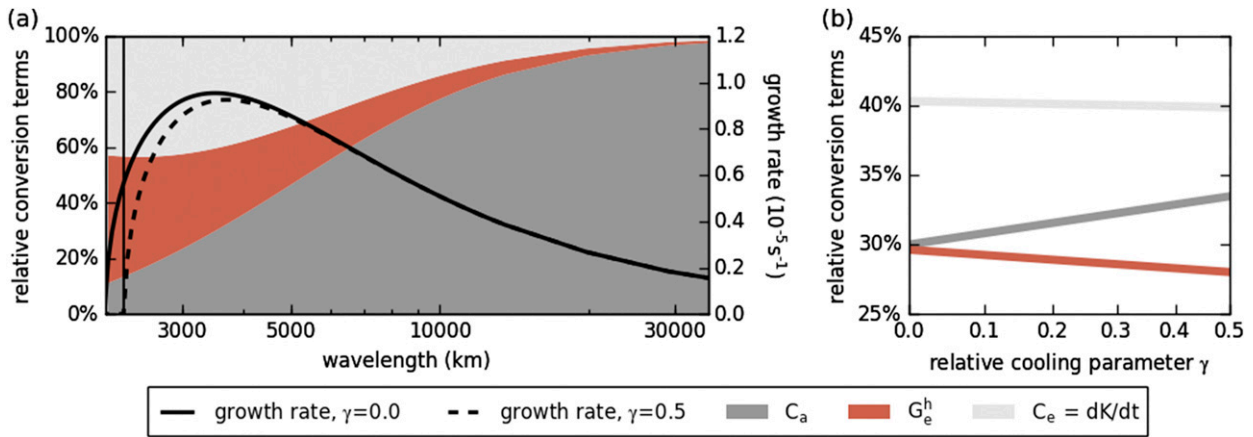


FIG. 10. Relative contributions to the energetics from  $C_a = -(\lambda/S)\overline{\psi_x\psi_p}$  (dark gray),  $G_e^h = -(1/S)\overline{Q\psi_p}$  (red), and  $C_e = \overline{\omega\psi_p}$  (light gray) (a) with corresponding growth rates for  $\gamma = 0.0$  (solid black) and  $\gamma = 0.5$  (dashed black) and (b) for the most unstable mode with varying  $\gamma$ . The energetics in (a) are valid for both  $\gamma = 0.0$  and  $\gamma = 0.5$ , but, as they can only be evaluated where the growth rate is nonzero, one should not consider the shading to the left of the shortwave cutoff (vertical line) for  $\gamma = 0.5$ . The change in the energetics with  $\gamma$  in (b) is only a result of the wavelength shift of the most unstable mode.

Although we find the contribution from  $G_e^c$  to be negligible (not shown), latent cooling still has an important indirect impact on the energetics through its modification of vertical motion and latent heating, and hence  $G_e^h$ .

The primary source of eddy available potential energy stems from  $G_e^h$  and  $C_e$  at short wavelengths and  $C_a$  at long wavelengths (Fig. 10), because  $G_e^h$  and  $C_e$  depend on the vertical motion, which is largest at short wavelengths (Fig. 9). Consistent with the decrease in vertical motion for increasing  $\gamma$  (Fig. 6c), the relative

importance of  $G_e^h$  and  $C_e$  decreases when latent cooling is included (Fig. 10b).

## 6. Sensitivity to heating profile

We investigate the sensitivity of our results to the shape of the idealized heating profile by diagnosing how the growth rate and structure respond to heating profiles that are more realistic than a step function. Motivated particularly by the heating distribution found in a simulation of a deep midlatitude cyclone studied by

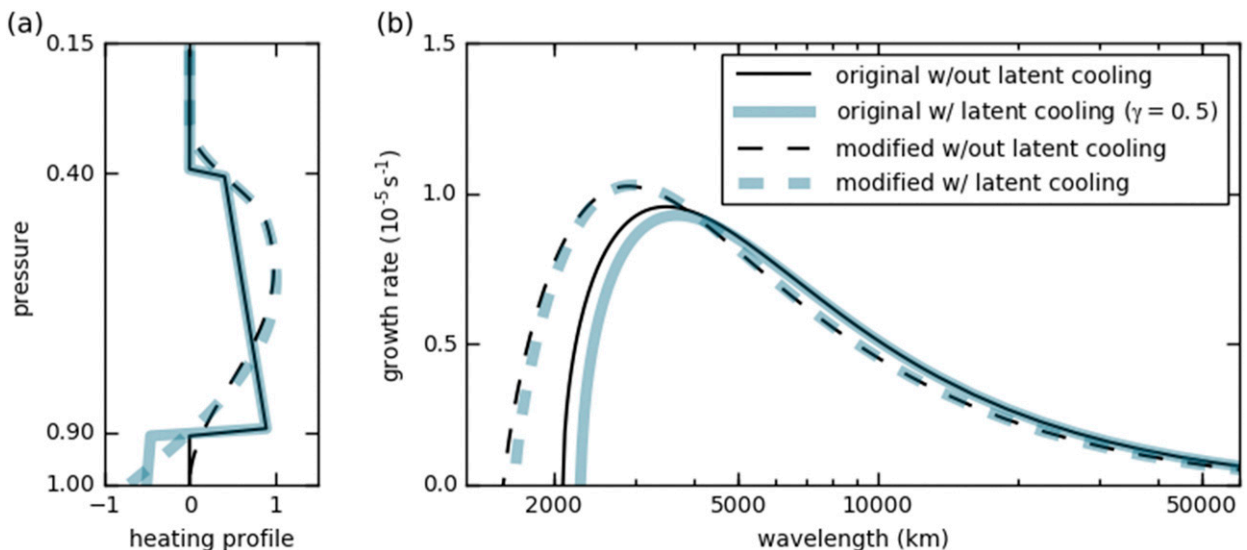


FIG. 11. (a) Original (solid) and modified (dashed) heating profiles  $\tilde{h}$  without latent cooling (black) and with latent cooling (blue,  $\gamma = 0.5$  in original profile) for  $\varepsilon = 12.5$ . See text for definition of profiles. (b) Growth rates corresponding to the heating profiles in (a) for varying wavelengths.

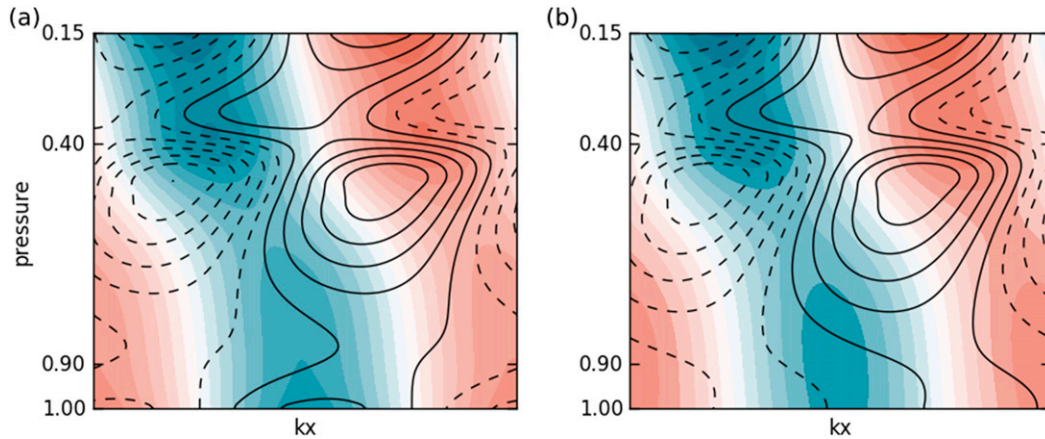


FIG. 12. Structure of streamfunction (shading) and temperature (contours) for the most unstable mode using the modified heating profiles in Fig. 11 with (a) latent heating only (dashed black profile in Fig. 11a), and (b) latent heating and cooling (dashed blue profile in Fig. 11a).

Dearden et al. (2016) as well as heating distributions from other case studies of midlatitude cyclones (e.g., Pauley and Nieman 1992; Joos and Forbes 2016), we devise the two modified heating profiles shown as dashed lines in Fig. 11a (see the appendix for details). Note that Fig. 11a shows the physical profile of heating  $\hat{h}$  obtained by multiplying the heating profile  $h$  with pressure  $p$  (see section 2b), yielding a better basis for comparison to the heating distribution in the previously mentioned case studies.

When using the modified profiles, the maximum growth rate is somewhat larger and shifted to shorter scales (see Fig. 11b), although latent cooling still has a stabilizing effect. The modified structures of the streamfunction and the temperature (Fig. 12) are smoother than the original structures shown in Fig. 5. However, they possess many of the same features, such as the collocation between warm (cold) air and upward (downward) motion (not shown), as well as the secondary maxima in the streamfunction at the top of the heating layer. The main difference is the shift from the two local maxima in temperature at the heating boundaries to one maximum around  $p = 0.5$ , as well as reduced maxima in temperature at the surface.

The structures of other quantities, such as vertical motion, diabatic heating, and meridional velocity, are also smoother but remain qualitatively similar when modifying the heating profile (not shown). These findings demonstrate that the idealized heating profile yields qualitatively meaningful results and that our interpretation is also applicable to more realistic heating profiles.

### 7. Sensitivity to static stability

So far, we assumed a constant basic-state static stability  $S$ . However, as argued by, for example, Lapeyre

and Held (2004) and O’Gorman (2011), the effective stratification reduces when the atmosphere is moist, because parcel displacements in the presence of latent heating and cooling are nearly moist adiabatic. To inspect whether these moist effects are accounted for in our model, we combine the terms involving static stability and diabatic heating in the thermodynamic equation

$$S\omega + \frac{\epsilon h \omega_{hb}}{2} = -\frac{RT_0}{p} \left( \frac{\partial \ln \theta_0}{\partial p} \omega + \frac{\partial F}{\partial p} \omega_{hb} \right) \neq -\frac{RT_0}{p} \frac{\partial (\ln \theta_0 + f)}{\partial p} \omega, \quad (14)$$

where  $\theta_0$  is the basic-state potential temperature and  $\partial F/\partial p = \{[-\epsilon h(p)]/2\}(p/RT_0) = (\partial f/\partial p)(\omega/\omega_{hb})$  represents the moist contribution to the effective stratification. Since the heating parameterization is based on  $\omega_{hb}$ , and not  $\omega$ , it is not straightforward to define an effective stratification expressed as the right-hand side of the inequality in (14). Furthermore, the effect of diabatic forcing on the effective stratification can be both positive and negative, depending on the sign of the heating profile  $h$ . The moist effects on stratification are thus only partly accounted for. We examine these effects further by testing the sensitivity of our results to changes in  $S$ . As we cannot accommodate any zonal variations of the basic-state static stability in our model, we reduce the stability in both the regions of ascent and descent in the baroclinic wave.

To test the sensitivity of our results to reduced stratification, we investigate how reducing the static stability by 25% affects the growth rates when latent heating and cooling are included. In addition to our reference profile  $S$ , we introduce

$$S_h = 4 - H(p - 0.41) + H(p - 0.89) \quad (15)$$

and

$$S_{hc} = 4 - H(p - 0.41), \quad (16)$$

where  $H$  is the Heaviside step function. These profiles prescribe reduced stability either in the heating layer only  $S_h$  or in the heating *and* the cooling layer  $S_{hc}$ . We argue that  $S_{hc}$  is most realistic, as the stratification below the heating layer is also nearly moist adiabatic because of evaporation and associated latent cooling. Note that the steps in static stability introduce PV anomalies and levels with basic-state meridional PV gradients because of the nonzero vertical gradients of  $S_h$  and  $S_{hc}$ .

When the static stability is reduced in parts of the model domain (profiles  $S_h$  and  $S_{hc}$ ), the growth rates increase and the most unstable solution moves to shorter wavelengths (Fig. 13). This is expected, because a reduced stability is associated with enhanced vertical interaction between PV anomalies. The growth rates increase most when the stability is reduced all the way down to the surface  $S_{hc}$ , which is due to a deeper layer of reduced stability and hence a greater net reduction of the overall stability. For all stability profiles, the growth rates decrease when latent cooling is included, in accordance with the results in section 3.

We also tested the impact of the vertical extent of the layer of reduced effective stratification by varying the location and the magnitude of the reduced stability (not shown). When the upper boundary of the layer of weaker stability is shifted from 410 to 500 hPa and/or the lower boundary is shifted from 890 to 800 hPa, the growth rates decrease, because the overall reduction of stability is weaker. Furthermore, when  $S_h$  and  $S_{hc}$  are adjusted so that the mean stability is identical for all profiles, the growth rates are largest when the stability is not constant, that is, for  $S_h$  and  $S_{hc}$ . For these cases, the increased growth rates cannot be explained by a net reduction of overall static stability and are more likely related to the superpositioning of the diabatic PV anomalies and the PV anomalies induced by the steps in the static stability profile. Independent of the changes in static stability in this section, the effect of latent cooling remains detrimental for baroclinic instability.

## 8. Concluding remarks

Including diabatic effects representing both midtropospheric latent heating and low-level latent cooling with heating intensities comparable to realistic midlatitude cyclones into the Eady model, we find that latent cooling reduces baroclinic growth and shifts the most unstable mode to longer wavelengths. For quantitative

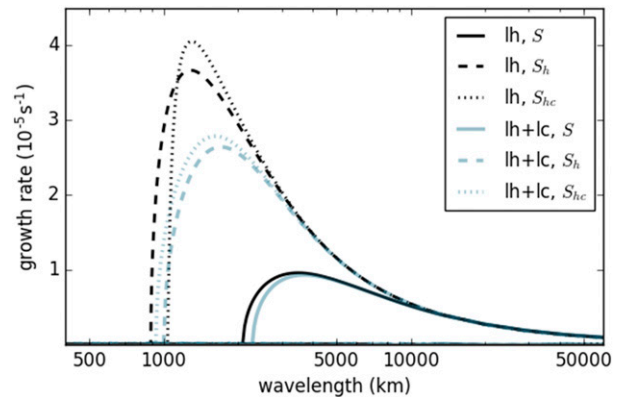


FIG. 13. Growth rates for various stability profiles:  $S$  (solid),  $S_h$  (dashed), and  $S_{hc}$  (dotted), for  $\varepsilon = 12.5$  and only latent heating (black,  $\gamma = 0.0$ ) as well as latent heating and cooling (blue,  $\gamma = 0.5$ ). See text for definition of stability profiles.

comparison, we normalize the results by total energy and find that the reduced growth is consistent with weakening both vertical motion and latent heating within the cyclone when low-level cooling is included. Thus, latent cooling is primarily an indirect effect that influences midlatitude cyclones by reducing the intensifying effect of latent heating.

The reduction of latent heating weakens the vertical heating gradients at the top and bottom of the heating layer and thus leads to weaker diabatically induced PV anomalies. The decrease in the vertical heating gradient at the bottom of the heating layer, however, is counteracted by the latent cooling below. Hence, the net change of the PV anomaly at the bottom of the heating layer depends on the relative contributions from the reduced latent heating above and latent cooling below. Nevertheless, the overall effect of latent cooling is an enhancement of the low-level PV anomaly *relative* to the PV anomaly at the top of the heating layer.

The direct contribution from latent cooling to the generation of eddy available potential energy is negligible. However, the contribution from latent heating decreases when latent cooling is included. Thus, the influence of latent cooling on cyclone development is primarily indirect through suppression of vertical motion and latent heating.

We obtain similar results when using heating profiles mimicking heating distributions from realistic case studies of midlatitude cyclones. Furthermore, when testing the sensitivity of our results to stability profiles that take into account that the effective static stability is reduced in a saturated moist atmosphere, the response to latent cooling remains qualitatively the same. The insensitivity to these variations proves the robustness of our results obtained with the idealized model setup.

Consistent with previous studies, our findings confirm that latent cooling enhances the low-level PV anomaly

in midlatitude cyclones for realistic heating intensities at the early development stage. Overall, however, we find that latent cooling is detrimental to cyclone development through reducing vertical motion and latent heating. These indirect effects should be further assessed using more complex three-dimensional models with the capacity to omit the effects of latent cooling to test their influence on cyclone development.

*Acknowledgments.* We thank Michael Reeder, Hylke de Vries, and Craig Bishop for valuable discussion

and comments. We also appreciate the comments by Mankin Mak and two anonymous reviewers. This work was supported by UNPACC (NFR Project 262220).

APPENDIX

Modified Heating Profiles

The modified heating profiles used for the sensitivity study in section 6 are

$$h(p) = \beta \times \begin{cases} 0 & \text{for } p < p_{ht} - \delta \\ \sin^2 \left\{ \frac{\pi[p - (p_{ht} - \delta)]}{2[(p_{ht} + \delta) - (p_{ht} - \delta)]} \right\} & \text{for } p_{ht} - \delta < p < p_{ht} + \delta \\ 1 & \text{for } p_{ht} + \delta < p < p_{hb^*} - \delta^* \\ \sin^2 \left\{ \frac{\pi[p - (p_{hb^*} + \delta^*)]}{2[(p_{hb^*} + \delta^*) - (p_{hb^*} - \delta^*)]} \right\} & \text{for } p_{hb^*} - \delta^* < p < p_{hb^*} + \delta^* \\ 0 & \text{for } p_{hb^*} + \delta^* < p \end{cases}, \tag{A1}$$

$$h(p) = \beta \times \begin{cases} 0 & \text{for } p < p_{ht} - \delta \\ \sin^2 \left\{ \frac{\pi[p - (p_{ht} - \delta)]}{2[(p_{ht} + \delta) - (p_{ht} - \delta)]} \right\} & \text{for } p_{ht} - \delta < p < p_{ht} + \delta \\ 1 & \text{for } p_{ht} + \delta < p < p_{hb^*} - \delta^* \\ \sin \left\{ \frac{\pi[p - p_{hb}]}{2[p_{hb^*} - \delta^* - p_{hb}]} \right\} & \text{for } p_{hb^*} - \delta^* < p, \end{cases} \tag{A2}$$

where the former (latter) excludes (includes) latent cooling at lower levels, and  $\delta$  ( $\delta^*$ ) determines the sharpness of the smooth curve around  $p = p_{ht}$  ( $p = p_{hb^*}$ ). The profiles shown in Fig. 11a are obtained by multiplying (A1) and (A2) by  $p$ , where  $\beta = 1.8$ ,  $\delta = 0.1$ ,  $\delta^* = 0.25$ , and  $p_{hb^*} = 0.75$ .

REFERENCES

Ahmadi-Givi, F., G. Graig, and R. Plant, 2004: The dynamics of a midlatitude cyclone with very strong latent-heat release. *Quart. J. Roy. Meteor. Soc.*, **130**, 295–323, <https://doi.org/10.1256/qj.02.226>.

Anderson, E., and Coauthors, 1999: *LAPACK Users' Guide*. 3rd ed. Society for Industrial and Applied Mathematics, 407 pp.

Barth, M. C., and D. B. Parsons, 1996: Microphysical processes associated with intense frontal rainbands and the effect of evaporation and melting on frontal dynamics. *J. Atmos. Sci.*, **53**, 1569–1586, [https://doi.org/10.1175/1520-0469\(1996\)053<1569:MPAWIF>2.0.CO;2](https://doi.org/10.1175/1520-0469(1996)053<1569:MPAWIF>2.0.CO;2).

Bretherton, F. P., 1966: Baroclinic instability and the short wavelength cut-off in terms of potential instability. *Quart. J. Roy. Meteor. Soc.*, **92**, 335–345, <https://doi.org/10.1002/qj.49709239303>.

Browning, K. A., 1990: Organization of clouds and precipitation in extratropical cyclones. *Extratropical Cyclones: The Erik Palmén Memorial Volume*, C. W. Newton and E. O. Holopainen, Eds., Amer. Meteor. Soc., 129–153.

Clough, S., and R. Franks, 1991: The evaporation of frontal and other stratiform precipitation. *Quart. J. Roy. Meteor. Soc.*, **117**, 1057–1080, <https://doi.org/10.1002/qj.49711750109>.

Craig, G., and H.-R. Cho, 1988: Cumulus heating and CISK in the extratropical atmosphere. Part I: Polar lows and comma clouds. *J. Atmos. Sci.*, **45**, 2622–2640, [https://doi.org/10.1175/1520-0469\(1988\)045<2622:CHACIT>2.0.CO;2](https://doi.org/10.1175/1520-0469(1988)045<2622:CHACIT>2.0.CO;2).

Crezee, B., H. Joos, and H. Wernli, 2017: The microphysical building blocks of low-level potential vorticity anomalies in an idealized extratropical cyclone. *J. Atmos. Sci.*, **74**, 1403–1416, <https://doi.org/10.1175/JAS-D-16-0260.1>.

Davis, C., and K. Emanuel, 1991: Potential vorticity diagnostics of cyclogenesis. *J. Atmos. Sci.*, **119**, 1929–1953, [https://doi.org/10.1175/1520-0493\(1991\)119<1929:PVD0C>2.0.CO;2](https://doi.org/10.1175/1520-0493(1991)119<1929:PVD0C>2.0.CO;2).

- Dearden, C., G. Vaughan, T. Tsai, and J.-P. Chen, 2016: Exploring the diabatic role of ice microphysical processes in two North Atlantic summer cyclones. *Mon. Wea. Rev.*, **144**, 1249–1272, <https://doi.org/10.1175/MWR-D-15-0253.1>.
- De Vries, H., J. Methven, T. H. Frame, and B. J. Hoskins, 2010: Baroclinic waves with parameterized effects of moisture interpreted using Rossby wave components. *J. Atmos. Sci.*, **67**, 2766–2784, <https://doi.org/10.1175/2010JAS3410.1>.
- Eady, E. T., 1949: Long-waves and cyclone waves. *Tellus*, **1** (3), 33–52, <https://doi.org/10.3402/tellusa.v1i3.8507>.
- Emanuel, K. A., M. Fantini, and A. J. Thorpe, 1987: Baroclinic instability in an environment of small stability to slantwise moist convection. Part I: Two-dimensional models. *J. Atmos. Sci.*, **44**, 1559–1573, [https://doi.org/10.1175/1520-0469\(1987\)044<1559:BIIAEO>2.0.CO;2](https://doi.org/10.1175/1520-0469(1987)044<1559:BIIAEO>2.0.CO;2).
- Forbes, R. M., and P. A. Clark, 2003: Sensitivity of extratropical cyclone mesoscale structure to the parametrization of ice microphysical processes. *Quart. J. Roy. Meteor. Soc.*, **129**, 1123–1148, <https://doi.org/10.1256/qj.01.171>.
- Heifetz, E., C. Bishop, B. Hoskins, and J. Methven, 2004: The counter-propagating Rossby-wave perspective on baroclinic instability. I: Mathematical basis. *Quart. J. Roy. Meteor. Soc.*, **130**, 211–231, <https://doi.org/10.1002/qj.200413059610>.
- Holton, J. R., and G. J. Hakim, 2012: *An Introduction to Dynamic Meteorology*. 5th ed. International Geophysics Series, Vol. 88, Academic Press, 532 pp.
- Hoskins, B. J., M. E. McIntyre, and A. W. Robertson, 1985: On the use and significance of isentropic potential vorticity maps. *Quart. J. Roy. Meteor. Soc.*, **111**, 877–946, <https://doi.org/10.1002/qj.49711147002>.
- Huang, H.-C., and K. A. Emanuel, 1991: The effects of evaporation on frontal circulations. *J. Atmos. Sci.*, **48**, 619–628, [https://doi.org/10.1175/1520-0469\(1991\)048<0619:TEOEOF>2.0.CO;2](https://doi.org/10.1175/1520-0469(1991)048<0619:TEOEOF>2.0.CO;2).
- Joos, H., and H. Wernli, 2012: Influence of microphysical processes on the potential vorticity development in a warm conveyor belt: A case-study with the limited-area model COSMO. *Quart. J. Roy. Meteor. Soc.*, **138**, 407–418, <https://doi.org/10.1002/qj.934>.
- , and R. M. Forbes, 2016: Impact of different IFS microphysics on a warm conveyor belt and the downstream flow evolution. *Quart. J. Roy. Meteor. Soc.*, **142**, 2727–2739, <https://doi.org/10.1002/qj.2863>.
- Kuo, Y.-H., M. Shapiro, and E. G. Donall, 1991: The interaction between baroclinic and diabatic processes in a numerical simulation of a rapidly intensifying extratropical marine cyclone. *Mon. Wea. Rev.*, **119**, 368–384, [https://doi.org/10.1175/1520-0493\(1991\)119<0368:TIBBAD>2.0.CO;2](https://doi.org/10.1175/1520-0493(1991)119<0368:TIBBAD>2.0.CO;2).
- Lapeyre, G., and I. M. Held, 2004: The role of moisture in the dynamics and energetics of turbulent baroclinic eddies. *J. Atmos. Sci.*, **61**, 1693–1710, [https://doi.org/10.1175/1520-0469\(2004\)061<1693:TROMIT>2.0.CO;2](https://doi.org/10.1175/1520-0469(2004)061<1693:TROMIT>2.0.CO;2).
- Lin, S. C., and P. J. Smith, 1979: Diabatic heating and generation of available potential energy in a tornado-producing extratropical cyclone. *Mon. Wea. Rev.*, **107**, 1169–1183, [https://doi.org/10.1175/1520-0493\(1979\)107<1169:DHAGOA>2.0.CO;2](https://doi.org/10.1175/1520-0493(1979)107<1169:DHAGOA>2.0.CO;2).
- Lorenz, E. N., 1955: Available potential energy and the maintenance of the general circulation. *Tellus*, **7**, 157–167, <https://doi.org/10.3402/tellusa.v7i2.8796>.
- Mak, M., 1994: Cyclogenesis in a conditionally unstable moist baroclinic atmosphere. *Tellus*, **46A**, 14–33, <https://doi.org/10.3402/tellusa.v46i1.15424>.
- Manabe, S., 1956: On the contribution of heat released by condensation to the change in pressure pattern. *J. Meteor. Soc. Japan*, **34**, 308–320, [https://doi.org/10.2151/jmsj1923.34.6\\_308](https://doi.org/10.2151/jmsj1923.34.6_308).
- Martínez-Alvarado, O., F. Weidle, and S. L. Gray, 2010: Sting jets in simulations of a real cyclone by two mesoscale models. *Mon. Wea. Rev.*, **138**, 4054–4075, <https://doi.org/10.1175/2010MWR3290.1>.
- , S. L. Gray, and J. Methven, 2016: Diabatic processes and the evolution of two contrasting summer extratropical cyclones. *Mon. Wea. Rev.*, **144**, 3251–3276, <https://doi.org/10.1175/MWR-D-15-0395.1>.
- Moore, R. W., and M. T. Montgomery, 2004: Reexamining the dynamics of short-scale, diabatic Rossby waves and their role in midlatitude moist cyclogenesis. *J. Atmos. Sci.*, **61**, 754–768, [https://doi.org/10.1175/1520-0469\(2004\)061<0754:RTDOSD>2.0.CO;2](https://doi.org/10.1175/1520-0469(2004)061<0754:RTDOSD>2.0.CO;2).
- O’Gorman, P. A., 2011: The effective static stability experienced by eddies in a moist atmosphere. *J. Atmos. Sci.*, **68**, 75–90, <https://doi.org/10.1175/2010JAS3537.1>.
- Parker, D. J., and A. J. Thorpe, 1995: Conditional convective heating in a baroclinic atmosphere: A model of convective frontogenesis. *J. Atmos. Sci.*, **52**, 1699–1711, [https://doi.org/10.1175/1520-0469\(1995\)052<1699:CCHIAB>2.0.CO;2](https://doi.org/10.1175/1520-0469(1995)052<1699:CCHIAB>2.0.CO;2).
- Pauley, P. M., and S. J. Nieman, 1992: A comparison of quasi-geostrophic and nonquasi-geostrophic vertical motions for a model-simulated rapidly intensifying marine extratropical cyclone. *Mon. Wea. Rev.*, **120**, 1108–1134, [https://doi.org/10.1175/1520-0493\(1992\)120<1108:ACOQAN>2.0.CO;2](https://doi.org/10.1175/1520-0493(1992)120<1108:ACOQAN>2.0.CO;2).
- Pomroy, H. R., and A. J. Thorpe, 2000: The evolution and dynamical role of reduced upper-tropospheric potential vorticity in intensive observing period one of FASTEX. *Mon. Wea. Rev.*, **128**, 1817–1834, [https://doi.org/10.1175/1520-0493\(2000\)128<1817:TEADRO>2.0.CO;2](https://doi.org/10.1175/1520-0493(2000)128<1817:TEADRO>2.0.CO;2).
- Rantanen, M., J. Räisänen, J. Lento, O. Stepanyuk, O. Räty, V. A. Sinclair, and H. Järvinen, 2017: OZO v. 1.0: Software for solving a generalised omega equation and the Zwack–Okossi height tendency equation using WRF Model output. *Geosci. Model Dev.*, **10**, 827–841, <https://doi.org/10.5194/gmd-10-827-2017>.
- Robertson, F., and P. Smith, 1983: The impact of model moist processes on the energetics of extratropical cyclones. *Mon. Wea. Rev.*, **111**, 723–744, [https://doi.org/10.1175/1520-0493\(1983\)111<0723:TROMMP>2.0.CO;2](https://doi.org/10.1175/1520-0493(1983)111<0723:TROMMP>2.0.CO;2).
- Smith, P. J., 1980: The energetics of extratropical cyclones. *Rev. Geophys.*, **18**, 378–386, <https://doi.org/10.1029/RG018i002p00378>.
- Snyder, C., and R. S. Lindzen, 1991: Quasi-geostrophic wave-CISK in an unbounded baroclinic shear. *J. Atmos. Sci.*, **48**, 76–86, [https://doi.org/10.1175/1520-0469\(1991\)048<0076:QGWICIA>2.0.CO;2](https://doi.org/10.1175/1520-0469(1991)048<0076:QGWICIA>2.0.CO;2).
- Stepanyuk, O., J. Räisänen, V. A. Sinclair, and H. Järvinen, 2017: Factors affecting atmospheric vertical motions as analyzed with a generalized omega equation and the OpenIFS model. *Tellus*, **69**, 1271563, <https://doi.org/10.1080/16000870.2016.1271563>.
- Stoelinga, M. T., 1996: A potential vorticity-based study of the role of diabatic heating and friction in a numerically simulated baroclinic cyclone. *Mon. Wea. Rev.*, **124**, 849–874, [https://doi.org/10.1175/1520-0493\(1996\)124<0849:APVBSO>2.0.CO;2](https://doi.org/10.1175/1520-0493(1996)124<0849:APVBSO>2.0.CO;2).
- Terpstra, A., T. Spengler, and R. W. Moore, 2015: Idealised simulations of polar low development in an Arctic moist baroclinic environment. *Quart. J. Roy. Meteor. Soc.*, **141**, 1987–1996, <https://doi.org/10.1002/qj.2507>.
- Vincent, D. G., G. B. Pant, and H. J. Edmon Jr., 1977: Generation of available potential energy of an extratropical cyclone system. *Mon. Wea. Rev.*, **105**, 1252–1265, [https://doi.org/10.1175/1520-0493\(1977\)105<1252:GOAPEO>2.0.CO;2](https://doi.org/10.1175/1520-0493(1977)105<1252:GOAPEO>2.0.CO;2).
- Whitaker, J. S., and C. A. Davis, 1994: Cyclogenesis in a saturated environment. *J. Atmos. Sci.*, **51**, 889–907, [https://doi.org/10.1175/1520-0469\(1994\)051<0889:CIASE>2.0.CO;2](https://doi.org/10.1175/1520-0469(1994)051<0889:CIASE>2.0.CO;2).